XFEM Analysis of Strain Localization on Hostun RF Sand using Integral Type Nonlocal Model

Meysam Zarinfar
PhD Candidate, Civil Engineering Department
K.N.Toosi University of Technology, Tehran, Iran
Corresponding author; e-mail: zarinfar@dena.kntu.ac.ir

Farzin Kalantary
Assistant Professor, Civil Engineering Department
K.N.Toosi University of Technology, Tehran, Iran
e-mail: fz_kalantary@yahoo.co.uk

ABSTRACT

Localization phenomena, as e.g. shear bands, is a narrow zone of local concentrations of plastic strains. The numerical methods that use the classical continuum models, suffer from the excessive mesh dependence when a strain-softening model is used. With a nonlocal formulation, this pathology is eliminated. In the present paper, a new relation was proposed to calculate the stress rate based on the integral-type nonlocal model. For nonlocal plasticity, element size had a critical effect on the solution. Sufficiently refined meshes were required for an accurate solution without mesh dependency. It was shown that an extended finite element method can be applied to the problem to decrease the required mesh density close to the localization band. A new method based on the local bifurcation theory was proposed for the initiation and growth criterion of the strain localization interface. Localization of deformation in biaxial tests on Hostun Rf sand were used to demonstrate the efficiency of the mixed XFEM–integral type nonlocal model in shear band localization modeling without mesh dependency. It was shown that shear banding can take place in both contractive and dilative specimens. Findings concerning the occurrence and progression of strain localization were discussed. Attention was laid on the influence of the mean effective stress and shear band orientation.

KEYWORDS: XFEM, Nonlocal plasticity, Shear band orientation, Mean effective stress, Biaxial tests

INTRODUCTION

Shear band localization refers to the localization of deformation into thin zones of intense shearing. This phenomenon is often accompanied with strain softening which means decrease of the load carrying capacity. Loret and Prevost [14], Sluys [19] and others have demonstrated that classical continuum theory is inadequate when localization phenomena occurs, since it leads to ill-posed problems in the numerical solution of the governing field equations.

In the framework of single phase solids, several numerical techniques have been proposed for strain localization problems, such as rate dependent constitutive models [14], gradient plasticity models [19], consideration of micropolar degrees of freedom [21] and non-local integral models [1, 22]. The localization problem of multiphase geomaterials was studied numerically using rate-dependent constitutive models [6], gradient plasticity models [23] and consideration of micropolar degrees of freedom [13]. The approach used here is the mixed XFEM and integral type nonlocal model. The nonlocal concept was first extended into continuum mechanics for plasticity by Eringen [7, 8]. Pijaudier-Cabot and Bazant [18] proposed using nonlocal treatment only for those variables that control the strain softening process. This formulation has the advantage that the differential equations of motion or equilibrium remain the same as in classical theory, without extra terms in the form of integrals or higher-order derivatives [2]. Jirasek [10] presented an overview of the integral-type nonlocal model for damage and fracture, Bazant and Jirasek [3] did for plasticity and damage, and Jirasek and Rolshoven [11] did for plasticity. It seems that formulations based on nonlocal averaging, widely used in single phase materials, have not been fully explored in the context of the multiphase porous media. In the present paper, a new relation is proposed to calculate the stress rate based on the integral-type nonlocal model. This relation depends on the local plastic strain rate and integral averaging of the local plastic strain rate. In the context of the nonlocal model, the mesh must be sufficiently refined near the high strain gradient region to resolve mesh dependency. The extended finite element method can be applied to decrease the required mesh density close to the shear band. The XFEM method, including the partition of unity concept, was discussed by Melenk and Babuska [16]. This technique was applied to crack growth problems by Belytschko and Black [4] and has been used successfully in the modeling of crack propagation. Fries and Belytschko [9] provided an overview of XFEM applications. This numerical strategy allows modeling of the mesh-independent approximation of the non-smooth solutions using enrichment functions which are close to the exact localization mode. In addition, the computational effort is reduced compared to remeshing methods. . In the present paper, a new method based on the local bifurcation theory is proposed for the initiation and growth criterion of the shear band localization interface. Localization starts when the ellipticity conditions of the static equation or the hyperbolicity of the dynamic equation are lost (onset of bifurcation) [2]. This condition is equivalent to zero or the negative determinant of the symmetric part of the acoustic tensor. Zarinfar and Kalantary [22] proposed the similar numerical algorithm for associated constitutive model. Strain localization begins at the first point in which the local criterion of bifurcation is satisfied. With continued loading, local criterion of bifurcation is satisfied in more points and thereafter strain localization grows inside the body.

The objective of the present paper is to propose a new numerical method for simulation of shear band localization in the nonlocal continuum mechanics of empty and fluid-saturated material without mesh dependency. Localization in multiphase materials is a challenging and difficult topic because it is not only influenced by the solid phase behavior but also by the fluid–solid interaction. No research was found using nonlocal integral models for numerical analysis of multiphase materials in the literature. In this paper, the XFEM formulation is presented in the framework of a generalized continuum model based on the nonlocal continuum theory, including the material length-scale parameter. The standard FE approximation is enriched by employing additional terms based on the hyperbolic tangent function. The interfaces of the localization band are represented independently of the element boundaries by XFEM. Local bifurcation is considered as a criterion for the initiation and growth of the strain localization interface. Most of the literature about nonlocal models deals with their mechanical and numerical implementation. But in order to judge the ability of a model to describe the mechanical behavior of a material comparisons of numerical calculations with results of laboratory tests are necessary. In order to

demonstrate the efficiency of the enhanced model, the results of biaxial tests on dense and loose Hostun RF sand under drained and undrained condition performed by Desrues and Viggiani [5] and Mokni and Desrues [17] are predicted with proposed model. The issues of shear band orientation, the effect of the mean stress and the initiation and the propagation of the shear bands are addressed.

GOVERNING EQUATIONS

Macroscopic balance equations for a saturated porous medium can be derived by the application of averaging theory to the microscopic balance equations of the constituents at microscopic level and introducing simplifying assumptions [12]. Isothermal conditions and compressible constituents were assumed for the present study. Convective acceleration terms, fluid density variation in space, and high frequency phenomena were neglected; such assumptions are common in soil mechanics [24]. The macroscopic balance equations in an updated Lagrangian framework consist of a linear momentum balance equation for saturated porous media, linear momentum balance equation (Darcy's law) for water species and mass balance.

$$\mathrm{div}\boldsymbol{\sigma} - \rho\ddot{\mathbf{u}} + \rho\mathbf{b} = 0 \tag{1}$$

$$\mathbf{w} = k(-\mathrm{grad}\mathbf{p} - \rho_f\ddot{\mathbf{u}} + \rho_f\mathbf{b}) \tag{2}$$

$$\frac{1}{Q^*}\dot{\mathbf{p}} + \alpha\mathrm{tr}\dot{\boldsymbol{\varepsilon}} + \mathrm{div}\mathbf{w} = 0 \tag{3}$$

where $\boldsymbol{\sigma} = \boldsymbol{\sigma}'' + \alpha\mathbf{p}\mathbf{I}$ is the total stress, $\boldsymbol{\sigma}''$ refers to the modified effective stress (Bishop's stress), $\mathbf{I}$ is the unit second-order tensor, $\mathbf{p}$ and $\mathbf{u}$ denote fluid pressure and displacement of solid skeleton, $\mathbf{w}$ is the average water velocity relative to the solid phase, k stands for the dynamic permeability, ρ and ρ_f are the mixture density and the fluid density respectively and the parameter $Q^* = \left[(\alpha - n)/k_s + n/k_f\right]^{-1}$,with k_s, k_f which are the bulk moduli of the solid and fluid phases respectively and n is the porosity. For an isotropic material the Biot's constant is $\alpha = k_T/k_s$ where k_T is the bulk moduli of the medium. In order to solve the governing equations, using the appropriate initial and boundary conditions is necessary. The Dirichlet boundary conditions are $\mathbf{u} = \bar{\mathbf{u}}$ on $\Gamma=\Gamma_{\mathbf{u}}$ and $\mathbf{p} = \bar{\mathbf{p}}$ on $\Gamma=\Gamma_{\mathbf{p}}$. The Neumann boundary conditions are $\mathbf{t} = \boldsymbol{\sigma}\mathbf{n} = \bar{\mathbf{t}}$ on $\Gamma=\Gamma_{\mathbf{t}}$ and $\mathbf{w}\mathbf{n} = \bar{\mathbf{w}}_n$ on $\Gamma= \Gamma_{\mathbf{w}}$.

XFEM FORMULATION OF DEFORMABLE SATURATED POROUS MEDIA

The spatial discretization involving the variables **u** and **p** is achieved by suitable shape functions. Therefore, the finite element polynomial displacement and pressure fields are enriched with regular Heaviside function which models the high displacement gradient in the localization band. The approximation of displacement (**u**) and pressure (**p**) fields can be expressed in the following form:

$$\mathbf{u}_{(\mathbf{x},t)} = \sum_{i=1}^{n_{nod}^{u}} N_{i(\mathbf{x})}^{u}\overline{\mathbf{u}}_{i(t)} + \sum_{i=1}^{n_{nod}^{u}} N_{i(\mathbf{x})}^{u}\left(R_{(\mathbf{x})}[\psi_{(\varphi(\mathbf{x}))} - \overline{\psi}_{(\varphi(\mathbf{x}_i))}]\overline{\mathbf{a}}_{i(t)}\right) = \sum_{i=1}^{n_{nod}^{u}} N_{i(\mathbf{x})}^{u}\overline{\mathbf{u}}_{i(t)} + \sum_{i=1}^{n_{nod}^{u}} N_{i(\mathbf{x})Enr}^{u}\overline{\mathbf{a}}_{i(t)} \quad (4)$$

$$\mathbf{p}_{(\mathbf{x},t)} = \sum_{i=1}^{n_{nod}^{p}} N_{i(\mathbf{x})}^{p}\overline{\mathbf{p}}_{i(t)} + \sum_{i=1}^{n_{nod}^{p}} N_{i(\mathbf{x})}^{p}\left(R_{(\mathbf{x})}[\psi_{(\varphi(\mathbf{x}))} - \overline{\psi}_{(\varphi(\mathbf{x}_i))}]\overline{\mathbf{b}}_{i(t)}\right) = \sum_{i=1}^{n_{nod}^{p}} N_{i(\mathbf{x})}^{p}\overline{\mathbf{p}}_{i(t)} + \sum_{i=1}^{n_{nod}^{u}} N_{i(\mathbf{x})Enr}^{p}\overline{\mathbf{b}}_{i(t)} \quad (5)$$

where n_{nod}^{u} and n_{nod}^{p} denote the number of element nodes, N_i^u and N_i^p the standard finite element shape function associated with node *i*, $\overline{\mathbf{u}}_i$ and $\overline{\mathbf{p}}_i$ the standard nodal displacement and pressure, $\overline{\mathbf{a}}_i$ and $\overline{\mathbf{b}}_i$ the additional degrees of freedom (DOF) associated with node *i*. In the above relation, $\psi_{(\mathbf{x})}$ denotes the appropriate enrichment function and $\varphi(\mathbf{x})$ is the distance from the strain localization interface. $R_{(x)}$ is the ramp function which resolves difficulties in blending elements [9].

$$R_{(\mathbf{x})} = \sum_{i}^{n_{enr}} N_{i(\mathbf{x})} \quad (6)$$

where n_{enr} is the number of enriched nodes of the element. This numerical technique improves the description of the displacement field inside the localized zone by adding the special enrichment functions which can model high gradient of displacement field. These functions and their gradients must be similar to the profile of displacement and strain fields. In this study, the hyperbolic tangent is employed to describe the corresponding profiles, as shown in Fig 1. This function is defined as:

$$\psi_{\varphi(x)} = tanh\left(2(\varphi(\mathbf{x}))/\beta\right) \quad (7)$$

where β is the parameter which controls width of the shear band. By selecting several values of β, one can construct a series of enrichment functions describing the displacement profile near the strain localization interface.
By substituting equation (4) in to strain rate definition, strain matrix can be defined as:

$$\dot{\boldsymbol{\varepsilon}} = \sum_{i=1}^{n_{nod}^{u}} \left[\mathbf{B}_{i(\mathbf{x})} \quad \mathbf{B}_{i(\mathbf{x})Enr}\right] \begin{bmatrix} \dot{\overline{\mathbf{u}}}_{i(t)} \\ \dot{\overline{\mathbf{a}}}_{i(t)} \end{bmatrix} \quad (8)$$

in which

$$\mathbf{B}_{i(\mathbf{x})} = \begin{bmatrix} \dfrac{\partial N_{i(\mathbf{x})}^{u}}{\partial x_1} & 0 \\ 0 & \dfrac{\partial N_{i(\mathbf{x})}^{u}}{\partial x_2} \\ \dfrac{\partial N_{i(\mathbf{x})}^{u}}{\partial x_2} & \dfrac{\partial N_{i(\mathbf{x})}^{u}}{\partial x_1} \end{bmatrix} \quad \mathbf{B}_{i(x)Enr} = \begin{bmatrix} \dfrac{\partial N_{i(\mathbf{x})Enr}^{u}}{\partial x_1} & 0 \\ 0 & \dfrac{\partial N_{i(\mathbf{x})Enr}^{u}}{\partial x_2} \\ \dfrac{\partial N_{i(\mathbf{x})Enr}^{u}}{\partial x_2} & \dfrac{\partial N_{i(\mathbf{x})Enr}^{u}}{\partial x_1} \end{bmatrix} \quad (9)$$

To obtain the weak form of the governing equations, Galerkin's procedure is used. The test functions $\delta \mathbf{u}(x,t)$ and $\delta\mathbf{p}(x,t)$ which have the same form as **u** and **p** are respectively multiplied by equations (1) and (3) and integrated over the domain Ω. Using the Divergence theorem leads to the following equations as:

$$\mathbf{M}\begin{bmatrix}\ddot{\bar{\mathbf{u}}}\\ \ddot{\bar{\mathbf{a}}}\end{bmatrix}+\int_\Omega \mathbf{B}^{\mathrm{T}}\boldsymbol{\sigma}''\mathrm{d}\Omega-\mathbf{Q}\begin{bmatrix}\bar{\mathbf{p}}\\ \bar{\mathbf{b}}\end{bmatrix}-\mathbf{F}^{(1)}=0 \tag{10}$$

$$\hat{\mathbf{Q}}\begin{bmatrix}\dot{\bar{\mathbf{u}}}\\ \dot{\bar{\mathbf{a}}}\end{bmatrix}+\mathbf{H}\begin{bmatrix}\bar{\mathbf{p}}\\ \bar{\mathbf{b}}\end{bmatrix}+\hat{\mathbf{S}}\begin{bmatrix}\dot{\bar{\mathbf{p}}}\\ \dot{\bar{\mathbf{b}}}\end{bmatrix}-\mathbf{F}^{(2)}=0 \tag{11}$$

in which

$$\mathbf{M}=\begin{bmatrix}\int_\Omega\left(\mathbf{N}^{\mathbf{u}}\right)^{\mathrm{T}}\rho\mathbf{N}^{\mathbf{u}}\mathrm{d}\Omega & \int_\Omega\left(\mathbf{N}^{\mathbf{u}}\right)^{\mathrm{T}}\rho\mathbf{N}^{\mathbf{u}}_{Enr}\mathrm{d}\Omega\\ \int_\Omega\left(\mathbf{N}^{\mathbf{u}}_{Enr}\right)^{\mathrm{T}}\rho\mathbf{N}^{\mathbf{u}}\mathrm{d}\Omega & \int_\Omega\left(\mathbf{N}^{\mathbf{u}}_{Enr}\right)^{\mathrm{T}}\rho\mathbf{N}^{\mathbf{u}}_{Enr}\mathrm{d}\Omega\end{bmatrix} \tag{12}$$

$$\mathbf{Q}=\begin{bmatrix}\int_\Omega\mathbf{B}^{T}\alpha\mathbf{m}\mathbf{N}^{p}\mathrm{d}\Omega & \int_\Omega\mathbf{B}^{T}\alpha\mathbf{m}\mathbf{N}^{p}_{Enr}\mathrm{d}\Omega\\ \int_\Omega\mathbf{B}^{T}_{Enr}\alpha\mathbf{m}\mathbf{N}^{p}\mathrm{d}\Omega & \int_\Omega\mathbf{B}^{T}_{Enr}\alpha\mathbf{m}\mathbf{N}^{p}_{Enr}\mathrm{d}\Omega\end{bmatrix} \tag{13}$$

$$\mathbf{F}^{(1)}=\begin{bmatrix}\int_\Omega\left(\mathbf{N}^{\mathbf{u}}\right)^{\mathrm{T}}\rho\mathbf{b}\mathrm{d}\Omega+\int_{\Gamma_{\mathrm{t}}}\left(\mathbf{N}^{\mathbf{u}}\right)^{\mathrm{T}}\bar{\mathbf{t}}\mathrm{d}\Gamma\\ \int_\Omega\left(\mathbf{N}^{\mathbf{u}}_{Enr}\right)^{\mathrm{T}}\rho\mathbf{b}\mathrm{d}\Omega+\int_{\Gamma_{\mathrm{t}}}\left(\mathbf{N}^{\mathbf{u}}_{Enr}\right)^{\mathrm{T}}\bar{\mathbf{t}}\mathrm{d}\Gamma\end{bmatrix} \tag{14}$$

$$\hat{\mathbf{Q}}=\begin{bmatrix}\int_\Omega\left(\mathbf{N}^{p}\right)^{T}\alpha\mathbf{m}^{T}\mathbf{B}\ \mathrm{d}\Omega & \int_\Omega\left(\mathbf{N}^{p}\right)^{T}\alpha\mathbf{m}^{T}\mathbf{B}_{Enr}\mathrm{d}\Omega\\ \int_\Omega\left(\mathbf{N}^{p}_{Enr}\right)^{T}\alpha\mathbf{m}^{T}\mathbf{B}\ \mathrm{d}\Omega & \int_\Omega\left(\mathbf{N}^{p}_{Enr}\right)^{T}\alpha\mathbf{m}^{T}\mathbf{B}_{Enr}\mathrm{d}\Omega\end{bmatrix} \tag{15}$$

$$\mathbf{H}=\begin{bmatrix}\int_\Omega\left(\nabla\mathbf{N}^{p}\right)^{T}\mathbf{k}\nabla\mathbf{N}^{p}\mathrm{d}\Omega & \int_\Omega\left(\nabla\mathbf{N}^{p}\right)^{T}\mathbf{k}\nabla\mathbf{N}^{p}_{Enr}\mathrm{d}\Omega\\ \int_\Omega\left(\nabla\mathbf{N}^{p}_{Enr}\right)^{T}\mathbf{k}\nabla\mathbf{N}^{p}\mathrm{d}\Omega & \int_\Omega\left(\nabla\mathbf{N}^{p}_{Enr}\right)^{T}\mathbf{k}\nabla\mathbf{N}^{p}_{Enr}\mathrm{d}\Omega\end{bmatrix} \tag{16}$$

$$\hat{\mathbf{S}}=\begin{bmatrix}\int_\Omega\left(\mathbf{N}^{p}\right)^{\mathrm{T}}\frac{1}{\mathrm{Q}^{*}}\mathbf{N}^{p}\mathrm{d}\Omega & \int_\Omega\left(\mathbf{N}^{p}\right)^{\mathrm{T}}\frac{1}{\mathrm{Q}^{*}}\mathbf{N}^{p}_{Enr}\mathrm{d}\Omega\\ \int_\Omega\left(\mathbf{N}^{p}_{Enr}\right)^{\mathrm{T}}\frac{1}{\mathrm{Q}^{*}}\mathbf{N}^{p}\mathrm{d}\Omega & \int_\Omega\left(\mathbf{N}^{p}_{Enr}\right)^{\mathrm{T}}\frac{1}{\mathrm{Q}^{*}}\mathbf{N}^{p}_{Enr}\mathrm{d}\Omega\end{bmatrix} \tag{17}$$

$$\mathbf{F}^{(2)}=\begin{bmatrix}-\int_\Omega\left(\nabla\mathbf{N}^{p}\right)^{\mathrm{T}}\mathbf{k}\rho_f\mathbf{b}\mathrm{d}\Omega+\int_{\Gamma_{\mathrm{w}}}\left(\mathbf{N}^{p}\right)^{\mathrm{T}}\bar{\mathbf{q}}\mathrm{d}\Gamma\\ -\int_\Omega\left(\nabla\mathbf{N}^{p}_{Enr}\right)^{\mathrm{T}}\mathbf{k}\rho_f\mathbf{b}\mathrm{d}\Omega+\int_{\Gamma_{\mathrm{w}}}\left(\mathbf{N}^{p}_{Enr}\right)^{\mathrm{T}}\bar{\mathbf{q}}\mathrm{d}\Gamma\end{bmatrix} \tag{18}$$

In the equations above, **m** is the vector defined as $\mathbf{m}^{\mathrm{T}}=[1\ 1\ 0\ ]$. The governing equations (10) and (11) are discretized in the time domain by means of the Newmark's scheme. The generalized Newmark GN22 method is employed for the displacement field (**u**,**a**) and GN11 method for the pressure field (**p**,**b**) as :

$$\begin{bmatrix}\dot{\bar{\mathbf{p}}}^{t+\Delta t}\\ \dot{\bar{\mathbf{b}}}^{t+\Delta t}\end{bmatrix}=\begin{bmatrix}\dot{\bar{\mathbf{p}}}^{t}+\Delta\dot{\bar{\mathbf{p}}}^{t}\\ \dot{\bar{\mathbf{b}}}^{t}+\Delta\dot{\bar{\mathbf{b}}}^{t}\end{bmatrix}\quad\begin{bmatrix}\bar{\mathbf{p}}^{t+\Delta t}\\ \bar{\mathbf{b}}^{t+\Delta t}\end{bmatrix}=\begin{bmatrix}\bar{\mathbf{p}}^{t}+\dot{\bar{\mathbf{p}}}^{t}\Delta t+\bar{\beta}\Delta\dot{\bar{\mathbf{p}}}^{t}\Delta t\\ \bar{\mathbf{b}}^{t}+\dot{\bar{\mathbf{b}}}^{t}\Delta t+\bar{\beta}\Delta\dot{\bar{\mathbf{b}}}^{t}\Delta t\end{bmatrix}\quad\begin{bmatrix}\ddot{\bar{\mathbf{u}}}^{t+\Delta t}\\ \ddot{\bar{\mathbf{a}}}^{t+\Delta t}\end{bmatrix}=\begin{bmatrix}\ddot{\bar{\mathbf{u}}}^{t}+\Delta\ddot{\bar{\mathbf{u}}}^{t}\\ \ddot{\bar{\mathbf{a}}}^{t}+\Delta\ddot{\bar{\mathbf{a}}}^{t}\end{bmatrix}$$

$$\begin{bmatrix}\dot{\bar{\mathbf{u}}}^{t+\Delta t}\\ \dot{\bar{\mathbf{a}}}^{t+\Delta t}\end{bmatrix}=\begin{bmatrix}\dot{\bar{\mathbf{u}}}^{t}+\ddot{\bar{\mathbf{u}}}^{t}\Delta t+\beta_1\Delta\ddot{\bar{\mathbf{u}}}^{t}\Delta t\\ \dot{\bar{\mathbf{a}}}^{t}+\ddot{\bar{\mathbf{a}}}^{t}\Delta t+\beta_1\Delta\ddot{\bar{\mathbf{a}}}^{t}\Delta t\end{bmatrix}\quad\begin{bmatrix}\bar{\mathbf{u}}^{t+\Delta t}\\ \bar{\mathbf{a}}^{t+\Delta t}\end{bmatrix}=\begin{bmatrix}\bar{\mathbf{u}}^{t}+\dot{\bar{\mathbf{u}}}^{t}\Delta t+\frac{1}{2}\ddot{\bar{\mathbf{u}}}^{t}\Delta t^2+\frac{1}{2}\beta_2\Delta\ddot{\bar{\mathbf{u}}}^{t}\Delta t^2\\ \bar{\mathbf{a}}^{t}+\dot{\bar{\mathbf{a}}}^{t}\Delta t+\frac{1}{2}\ddot{\bar{\mathbf{a}}}^{t}\Delta t^2+\frac{1}{2}\beta_2\Delta\ddot{\bar{\mathbf{a}}}^{t}\Delta t^2\end{bmatrix}\tag{19}$$

$\bar{\beta},\beta_1$ and β_2 are the Newmark parameters. For unconditional stability of the numerical procedure, it is required that $\bar{\beta}\geq.5$ and $\beta_2\geq\beta_1\geq.5$. It must be noted that equation 19 is obtained at the known time t i.e. $\dot{\bar{\mathbf{p}}}^{t},\bar{\mathbf{p}}^{t},\ddot{\bar{\mathbf{u}}}^{t},\dot{\bar{\mathbf{u}}}^{t}$ and $\bar{\mathbf{u}}^{t}$ are the known values of pressure and displacement field. Substituting relation (19) into the space-discrete equations (10) and (11), the following nonlinear equation can be achieved.

$$\begin{bmatrix}\mathbf{M}+.5\beta_2\Delta t^2\mathbf{K} & -\bar{\beta}\Delta t\mathbf{Q}\\ \beta_1\Delta t\hat{\mathbf{Q}} & \hat{\mathbf{S}}+\bar{\beta}\Delta t\mathbf{H}\end{bmatrix}\begin{bmatrix}\Delta\ddot{\bar{\mathbf{u}}}^{t}\\ \Delta\ddot{\bar{\mathbf{a}}}^{t}\\ \Delta\dot{\bar{\mathbf{p}}}^{t}\\ \Delta\dot{\bar{\mathbf{b}}}^{t}\end{bmatrix}=\begin{bmatrix}-\boldsymbol{\Psi}^{1}\\ -\boldsymbol{\Psi}^{2}\end{bmatrix}\tag{20}$$

In above equation, $\boldsymbol{\Psi}^{1}$ and $\boldsymbol{\Psi}^{2}$ denotes the vector of known values at time t and $\mathbf{K}$ is the tangential stiffness matrix.

$$\begin{aligned}\boldsymbol{\Psi}^{1}&=\mathbf{M}\begin{bmatrix}\ddot{\bar{\mathbf{u}}}^{t}\\ \ddot{\bar{\mathbf{a}}}^{t}\end{bmatrix}+\mathbf{K}\begin{bmatrix}\bar{\mathbf{u}}^{t}+\dot{\bar{\mathbf{u}}}^{t}\Delta t+.5\ddot{\bar{\mathbf{u}}}^{t}\Delta t^2\\ \bar{\mathbf{a}}^{t}+\dot{\bar{\mathbf{a}}}^{t}\Delta t+.5\ddot{\bar{\mathbf{a}}}^{t}\Delta t^2\end{bmatrix}-\mathbf{Q}\begin{bmatrix}\bar{\mathbf{p}}^{t}+\dot{\bar{\mathbf{p}}}^{t}\Delta t\\ \bar{\mathbf{b}}^{t}+\dot{\bar{\mathbf{b}}}^{t}\Delta t\end{bmatrix}-\left(\mathbf{F}^{1}\right)^{t+\Delta t}\\ \boldsymbol{\Psi}^{2}&=\hat{\mathbf{Q}}\begin{bmatrix}\dot{\bar{\mathbf{u}}}^{t}+\ddot{\bar{\mathbf{u}}}^{t}\Delta t\\ \dot{\bar{\mathbf{a}}}^{t}+\ddot{\bar{\mathbf{a}}}^{t}\Delta t\end{bmatrix}+\mathbf{H}\begin{bmatrix}\bar{\mathbf{p}}^{t}+\dot{\bar{\mathbf{p}}}^{t}\Delta t\\ \bar{\mathbf{b}}^{t}+\dot{\bar{\mathbf{b}}}^{t}\Delta t\end{bmatrix}+\hat{\mathbf{S}}\begin{bmatrix}\dot{\bar{\mathbf{p}}}^{t}\\ \dot{\bar{\mathbf{b}}}^{t}\end{bmatrix}-\left(\mathbf{F}^{2}\right)^{t+\Delta t}\end{aligned}\tag{21}$$

$$\mathbf{K}=\frac{d\left(\int_\Omega\mathbf{B}^{\mathbf{T}}\boldsymbol{\sigma}'\mathrm{d}\Omega\right)}{d(\mathbf{u},\mathbf{a})}=\begin{bmatrix}\int_\Omega\mathbf{B}^{T}\mathbf{D}\ \mathbf{B}\ \mathrm{d}\Omega & \int_\Omega\mathbf{B}^{T}\mathbf{D}\ \mathbf{B}_{Enr}\mathrm{d}\Omega\\ \int_\Omega\mathbf{B}_{Enr}^{T}\mathbf{D}\ \mathbf{B}\ \mathrm{d}\Omega & \int_\Omega\mathbf{B}_{Enr}^{T}\mathbf{D}\ \mathbf{B}_{Enr}\mathrm{d}\Omega\end{bmatrix}\tag{22}$$

where $\mathbf{D}$ is the appropriate constitutive matrix. The non-linear coupled equation system is linearized in a standard way thus yielding the linear algebraic equation system (20) which can be solved using an appropriate approach, such as the Newton-Raphson procedure.

THE MIXED XFEM - INTEGRAL TYPE NONLOCAL FORMULATION

Nonlocal continuum theory uses integral averaging of the variable around its neighborhood, instead of a local definition. For example, nonlocal averaging of plastic strain tensor ($\bar{\varepsilon}_{ij}^{p}$) at location x may be defined by the local plastic strain tensor (ε_{ij}^{p}).

$$\bar{\varepsilon}_{ij}^{p}(\mathbf{x}) = \int_V \alpha'(\mathbf{x},\boldsymbol{\xi})\varepsilon_{ij}^{p}(\boldsymbol{\xi})dV \tag{23}$$

where V denotes volume of the body, $\alpha'(\mathbf{x},\boldsymbol{\xi})$ is suitable weighting function. In this paper Gaussian distribution function is used as a weighting function.

$$\alpha'(\mathbf{x},\boldsymbol{\xi}) = \frac{e^{-(2|\boldsymbol{\xi}-\mathbf{x}|/\gamma)^2}}{\int_V e^{-(2|\boldsymbol{\zeta}-\mathbf{x}|/\gamma)^2} dV} \tag{24}$$

in which γ is a scalar which is related to material length scale parameter. For numerical finite element computation, the integral definition (23) can be approximated by summation relation. As a conclusion, nonlocal plastic strain tensor can be written as follow:

$$\bar{\varepsilon}_{ij}^{p}(\mathbf{x}) = \sum_k \alpha'(\mathbf{x},\mathbf{x}_k)\varepsilon_{ij}^{p}(\mathbf{x}_k) \tag{25}$$

where k denotes gauss points which are closer to point $\mathbf{x}$ than 2γ. The value of $\alpha'(\mathbf{x},\boldsymbol{\xi})$ for gauss points with greater distance than2γ is negligible.
In this paper, equation (26) is proposed to calculate the effective stress vector rate from the local and nonlocal plastic strain vector rate.

$$\dot{\boldsymbol{\sigma}}'' = \mathbf{D}^{\mathbf{e}}\dot{\boldsymbol{\varepsilon}} - (1-m)\mathbf{D}^{\mathbf{e}}\dot{\boldsymbol{\varepsilon}}^{\mathbf{p}} - m\mathbf{D}^{\mathbf{e}}\dot{\bar{\boldsymbol{\varepsilon}}}^{\mathbf{p}} \tag{26}$$

where $\mathbf{D}^{e}$ is linear elastic matrix and m is a constant parameter. Using equation (26), the stress rate at a certain point is related to the plastic strain rate in its neighborhood. If the local plastic strain distribution in a body is smooth, nonlocal plastic strain is approximately equal to local plastic strain; thus, it can be concluded that the proposed formulation is approximately identical to the local formulation. When the distribution of local plastic strain becomes non-smooth, the difference between nonlocal plastic strain and local definition increases and differences between the two formulations are revealed. The formulation presented by Bazant and Lin [2] is a special case of equation (26) where m is considered to be 1; therefore, different patterns for the load-displacement curve can be obtained by changing m. This allows simulation of a wider range of materials. Since the proposed stress-strain relation uses a combination of local and nonlocal plastic strains, this formulation acts as a localization limiter [11]. The value of mE/H in which E denotes the elastic modulus should remain constant during loading to prevent numerical locking. Thus, the model describes the complete loss of material resistance without artificial locking effects.

Since the dissipative energy function is defined in local space, as in classic continuum mechanics, the associated flow rule can be used [11]. As a result, local plastic strain rate is obtained by equation (27).

$$\dot{\boldsymbol{\varepsilon}}^{\mathbf{p}} = \dot{\lambda}\frac{\partial F}{\partial \boldsymbol{\sigma}} \tag{27}$$

where $\dot{\lambda}$ denotes the plastic multiplier and F the yield function which can be defined as: $\mathrm{F}(\boldsymbol{\sigma},\kappa)=\mathrm{f}(\boldsymbol{\sigma})-\kappa=0$ in which κ is the hardening-softening parameter. Applying the consistency condition to the yield function, $\dot{\lambda}$ can be calculated as:

$$\dot{\lambda}=\frac{\left(\partial F/\partial\boldsymbol{\sigma}\right)^{T}\mathbf{D}^{e}}{H+\left(\partial F/\partial\boldsymbol{\sigma}\right)^{T}\mathbf{D}^{e}\left(\partial F/\partial\boldsymbol{\sigma}\right)}\dot{\boldsymbol{\varepsilon}} \tag{28}$$

where *H* denotes the plastic tangential modulus and is equal to $-\left(\partial F/\partial\kappa\right)\left(\partial\kappa/\partial\boldsymbol{\varepsilon}^{p}\right)$. By substituting equations (28) in to (27), vector form of plastic strain rate is obtained as a function of total strain vector rate.

$$\dot{\boldsymbol{\varepsilon}}^{\mathrm{p}}=\frac{\partial\mathrm{F}/\partial\boldsymbol{\sigma}\left(\partial\mathrm{F}/\partial\boldsymbol{\sigma}\right)^{\mathrm{T}}\mathbf{D}^{\mathbf{e}}}{\mathrm{H}+\left(\partial\mathrm{F}/\partial\boldsymbol{\sigma}\right)^{\mathrm{T}}\mathbf{D}^{\mathbf{e}}\left(\partial\mathrm{F}/\partial\boldsymbol{\sigma}\right)}\dot{\boldsymbol{\varepsilon}}=\Lambda\dot{\boldsymbol{\varepsilon}} \tag{29}$$

By using equations (25), (26) and (29), stress rate at gauss point *k* can be defined by:

$$\dot{\boldsymbol{\sigma}}_{k}''=\mathbf{D}_{k}^{\mathrm{e}}\left(\mathbf{I}-(1-\mathrm{m})\boldsymbol{\Lambda}_{k}\right)\dot{\boldsymbol{\varepsilon}}_{k}-\mathrm{m}\mathbf{D}_{k}^{\mathrm{e}}\left(\sum_{l}\boldsymbol{\Lambda}_{l}\,\alpha'\left(\mathbf{x}_{k},\mathbf{x}_{l}\right)\dot{\boldsymbol{\varepsilon}}_{l}\right) \tag{30}$$

where **I** is identity matrix and *l* denotes gauss points which are closer to gauss point *k* than 2*γ*. The tangent stiffness matrix (equation (22)) for mixed XFEM-integral type nonlocal plasticity for a specified element can be modified using numerical integration and Eq. (30).

$$\begin{aligned}\mathbf{K}=&\sum_{k}\left|J\right|W_{k}\begin{bmatrix}\mathbf{B}_{(\mathrm{x_k})}^{\mathrm{T}}\mathbf{D}_{\mathrm{k}}^{\mathrm{e}}\left(\mathrm{I}-\boldsymbol{\Lambda}_{\mathrm{k}}\right)\mathbf{B}_{(\mathrm{x_k})} & \mathbf{B}_{(\mathrm{x_k})}^{\mathrm{T}}\mathbf{D}_{\mathrm{k}}^{\mathrm{e}}\left(\mathrm{I}-\boldsymbol{\Lambda}_{\mathrm{k}}\right)\mathbf{B}_{(\mathrm{x_k})\mathrm{Enr}}\\ \mathbf{B}_{(\mathrm{x_k})\mathrm{Enr}}^{\mathrm{T}}\mathbf{D}_{\mathrm{k}}^{\mathrm{e}}\left(\mathrm{I}-\boldsymbol{\Lambda}_{\mathrm{k}}\right)\mathbf{B}_{(\mathrm{x_k})} & \mathbf{B}_{(\mathrm{x_k})\mathrm{Enr}}^{\mathrm{T}}\mathbf{D}_{\mathrm{k}}^{\mathrm{e}}\left(\mathrm{I}-\boldsymbol{\Lambda}_{\mathrm{k}}\right)\mathbf{B}_{(\mathrm{x_k})\mathrm{Enr}}\end{bmatrix}+\ldots\\ \ldots+\mathrm{m}&\sum_{k}\left|J\right|W_{k}\begin{bmatrix}\mathbf{B}_{(\mathrm{x_k})}^{\mathrm{T}}\mathbf{D}_{\mathrm{k}}^{\mathrm{e}}\left(\boldsymbol{\Lambda}_{\mathrm{k}}\right)\mathbf{B}_{(\mathrm{x_k})} & \mathbf{B}_{(\mathrm{x_k})}^{\mathrm{T}}\mathbf{D}_{\mathrm{k}}^{\mathrm{e}}\left(\boldsymbol{\Lambda}_{\mathrm{k}}\right)\mathbf{B}_{(\mathrm{x_k})\mathrm{Enr}}\\ \mathbf{B}_{(\mathrm{x_k})\mathrm{Enr}}^{\mathrm{T}}\mathbf{D}_{\mathrm{k}}^{\mathrm{e}}\left(\boldsymbol{\Lambda}_{\mathrm{k}}\right)\mathbf{B}_{(\mathrm{x_k})} & \mathbf{B}_{(\mathrm{x_k})\mathrm{Enr}}^{\mathrm{T}}\mathbf{D}_{\mathrm{k}}^{\mathrm{e}}\left(\boldsymbol{\Lambda}_{\mathrm{k}}\right)\mathbf{B}_{(\mathrm{x_k})\mathrm{Enr}}\end{bmatrix}+\ldots\\ \ldots-\mathrm{m}&\sum_{k}\sum_{l}\left|J\right|W_{k}\begin{bmatrix}\mathbf{B}_{(\mathrm{x_k})}^{\mathrm{T}}\mathbf{D}_{\mathrm{k}}^{\mathrm{e}}\left(\boldsymbol{\Lambda}_{l}\right)\alpha'\left(\mathbf{x}_{\mathrm{k}},\mathbf{x}_{l}\right)\mathbf{B}_{(\mathrm{x_l})} & \mathbf{B}_{(\mathrm{x_k})}^{\mathrm{T}}\mathbf{D}_{\mathrm{k}}^{\mathrm{e}}\left(\boldsymbol{\Lambda}_{l}\right)\alpha'\left(\mathbf{x}_{\mathrm{k}},\mathbf{x}_{l}\right)\mathbf{B}_{(\mathrm{x_l})\mathrm{Enr}}\\ \mathbf{B}_{(\mathrm{x_k})\mathrm{Enr}}^{\mathrm{T}}\mathbf{D}_{\mathrm{k}}^{\mathrm{e}}\left(\boldsymbol{\Lambda}_{l}\right)\alpha'\left(\mathbf{x}_{\mathrm{k}},\mathbf{x}_{l}\right)\mathbf{B}_{(\mathrm{x_l})} & \mathbf{B}_{(\mathrm{x_k})\mathrm{Enr}}^{\mathrm{T}}\mathbf{D}_{\mathrm{k}}^{\mathrm{e}}\left(\boldsymbol{\Lambda}_{l}\right)\alpha'\left(\mathbf{x}_{\mathrm{k}},\mathbf{x}_{l}\right)\mathbf{B}_{(\mathrm{x_l})\mathrm{Enr}}\end{bmatrix}\end{aligned} \tag{31}$$

where $\left|J\right|$ is determinant of Jacobian matrix and W_k denotes weight coefficient of the gaussian quadrature. If the second and third terms in equation (31) are ignored, the formulation becomes equivalent to local theory. The DOF of one element may become related to the DOF of a non-neighboring element because of the third term of equation (31). In conclusion, the nonzero components of the tangent stiffness matrix increase. In this situation, the tangent stiffness matrix is not symmetrical because $\alpha(\mathbf{x}_k, \mathbf{x}_l) \neq \alpha(\mathbf{x}_l, \mathbf{x}_k)$.

DETERMINATION OF STRAIN LOCALIZATION INTERFACE

By applying enrichment functions to the formulation, additional DOF must be assigned to the nodes. At the beginning of the analysis, the additional DOF are inactive. For this reason a criterion must be defined for the activation of additional DOF. This study proposed the local bifurcation criterion to locate strain localization interface. Zarinfar and Kalantary [22] proposed the similar numerical algorithm for associated constitutive model. But in the case of a non associated constitutive model, this criterion coincides with the singularity of the symmetric part of the acoustic tensor [20]. Acoustic tensor can be defined as:

$$A_{ij} = C^{ep}_{ikjl} n_k n_l \tag{32}$$

where n is a unit vector and C^{ep}_{ikjl} denotes local elasto-plastic constitutive tensor.

$$C^{ep}_{ikjl} = C^{e}_{ikjl} - \frac{C^{e}_{ikmn}\,\partial F/\partial\sigma_{mn} C^{e}_{pqjl}\,\partial F/\partial\sigma_{pq}}{\left(H + \partial F/\partial\sigma_{rs} C^{e}_{rstu}\,\partial F/\partial\sigma_{tu}\right)} \tag{33}$$

If there is a direction in which the determinant of the symmetric part of the acoustic tensor becomes zero or negative, strain localization probably starts, and XFEM must be used to approximate the displacement field. At each Gauss point, then, a direction must be found in which the determinant of tensor has the lowest value. One independent variable is sufficient to describe unit vector n in two-dimensional space. As a result, this determinant is a function of one variable, and its lowest value can easily be calculated. This approach allows us to identify points where strain localization is likely to occur.

In order to perform the numerical algorithm, it is assumed that the interface, i.e. the centerline of the localization zone, and the Gauss points which have a negative determinant of the symmetric part of the acoustic tensor are known at time t (Fig. 2). Moreover, the vector V corresponding to the minimum determinant at the last point of the interface, i.e. L, is known at time t.

The vector V' is plotted from L to the Gauss point which has a negative determinant of the symmetric part of the acoustic tensor, i.e. G. Then the angle between V and V' is obtained. The next point for the centerline of the localization zone is a Gauss point whose corresponding vector V' has a minimum angle with V. Once the new interface is detected, additional DOF are activated at every nodal point whose support has an intersection with the enriched zone. If convergency is obtained at the end of the increment, the evolution of shear band is carried out to obtain the new interface for the next loading step. This technique is simple and has been employed in the examples. To avoid doubling back on the original path, the angle between the pieces of strain localization interface must be less than 90 degrees.

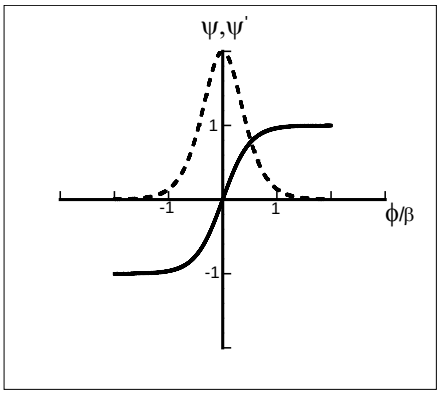

Figure 1: The smoothed hyperbolic tangent function and its derivative

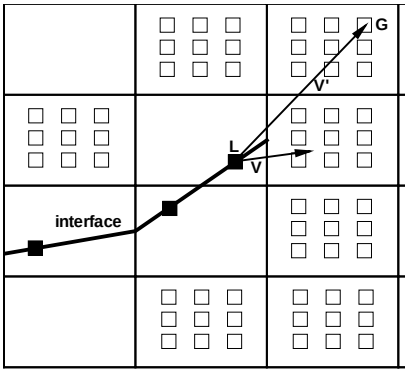

Figure 2: computational algorithm for the localization interface growth at step *n*

NUMERICAL SIMULATION

In order to demonstrate a part of the wide range of problems that can be solved by the present approach, we have illustrated the effective performance of XFEM technique using the integral type nonlocal continuum in strain localization analysis. A computer program is developed to investigate the computational aspects of the enriched finite element model in a higher order continuum model. The finite element mesh employed in all simulations is eight-noded rectangular plane strain elements with nine integration points. The analysis starts with the standard FE model with no enrichment functions. The enrichment function is then implemented into the standard shape functions by tracing the evolution of shear band zone. The parameter β, which is defined the width of enrichment zone, is set to γ in all analyzes due to the fact that the shear band thickness is about γ. All elements closer to the strain localization interface than β are enriched by the hyperbolic tangent function.

Comparison of the nonlocal and mixed XFEM-nonlocal model

In this example, the performance of the nonlocal formulation and mixed nonlocal-XFEM formulation were compared for fluid-saturated material. The geometry and boundary condition of biaxial test are shown in Fig. 3. The specimen is kept fixed horizontally and vertically in the middle of the bottom in order to preserve the stability of the specimen against sliding. The other nodes at the bottom are fixed vertically. Axial compression is applied to the specimen by vertical velocity (.1mm/s) of the top nodes. A Drucker-Prager yield criterion with associative flow rule and isotropic linear softening is used for the solid skeleton. The material parameters used during the computations are Young's modulus E=30 MPa, Poisson's ratio υ= 0.3, solid grain density ρ_s =2000 kg/m^3, water density ρ_w=998.2 kg/m^3, apparent cohesion c_0=0.5 MPa, hardening modulus H = -1 MPa, angle of internal friction φ= 10°, initial porosity n= 0:20, solid grain bulk modulus K_s= 6.78 GPa, water bulk modulus K_w= 0.20 GPa, permeability k= 5E-8 m/s. The shaded area of the specimen is taken as the weak zone, as shown in Fig 3. The initial apparent cohesion of this zone is assumed be equal to 60 percent of the apparent cohesion in other parts of the specimen. The parameter γ is set to 1cm and m is set to 1.5 to obtain the shear band thickness equal to 2.5 cm.

In order to show the capability of the non local extension with XFEM, the numerical results obtained with three different meshes are presented. The meshes consist of 120, 340 and 480 elements. Fig. 4 and Fig. 5 present the nonlocal effective plastic strain and pressure contours for both formulations. As seen, the results for coarse mesh are different than for other mesh results in the nonlocal formulation. In this formulation, thickness and inclination of the localization band depend on the mesh size. In the proposed approach, good agreement can be observed between the three mesh sizes; therefore, the XFEM can be applied to the problem to decrease the required mesh density close to the localization band. These figures confirm that the mixed nonlocal XFEM technique gives a good prediction of localization, even for the coarse mesh. As seen in Fig. 5, water pressure concentration with lower values can be observed at the centre of the shear bands due to the plastic dilatant behavior of the sand.

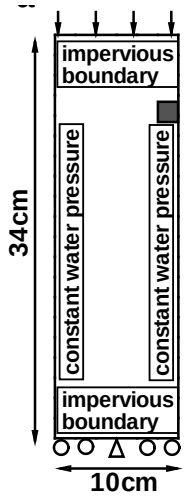

Figure 3: The biaxial specimen; the geometry and boundary conditions

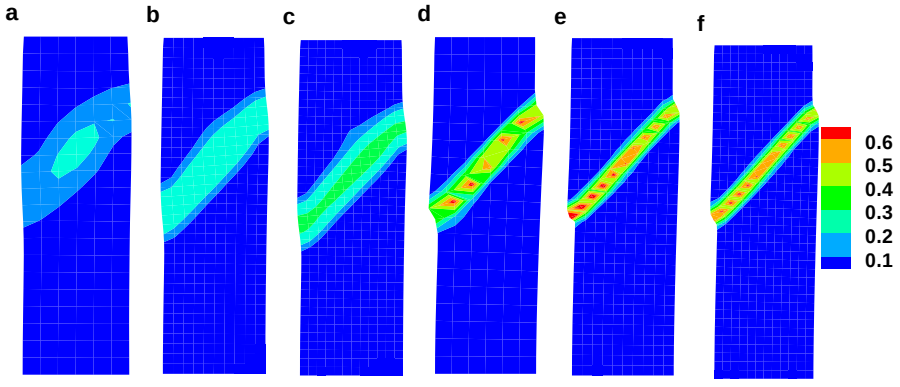

Figure 4: The effective plastic strain contour from; a,b,c) nonlocal model and d,e,f) mixed XFEM-nonlocal model; a,d) coarse mesh b,e)medium mesh c,f) fine mesh

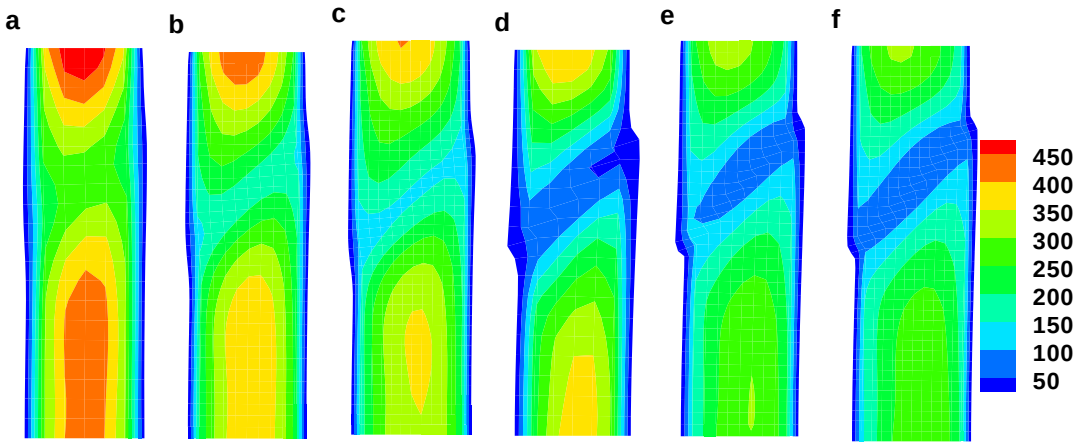

Figure 5: The distribution of pressure from; a,b,c) nonlocal model and d,e,f) mixed XFEM-nonlocal model; a,d) coarse mesh b,e) medium mesh c,f) fine mesh

Simulation of plane strain biaxial tests on dense and loose Hostun RF sand under drained and undrained condition

In the following the results of plane strain biaxial tests on dense and loose Hostun RF sand performed by Desrues and Viggiani [5], Mokni and Desrues [17] will be compared with numerical calculations done with the integral type nonlocal model enhanced by XFEM. Numerical calculations of plane strain compression tests were performed with a specimen which was 34 cm high and 10 cm wide. The geometry and boundary condition of biaxial test are shown in Fig. 6. The specimen is kept fixed horizontally and vertically in the middle of the bottom in order to preserve the stability of the specimen against sliding. The other nodes at the bottom are fixed vertically. Axial compression is applied to the specimen by vertical velocity (1.2mm/min) of the top nodes.

A Drucker-Prager yield criterion and isotropic linear softening is used. The weak imperfection is introduced in the top right part of the specimen to trigger numerically a shear band. The imperfection has got the size of four elements. The initial apparent cohesion of this zone is assumed be equal to 60 percent of the apparent cohesion in other parts of the specimen. The material parameters used during the computations are Poisson's ratio υ= 0.4, solid grain density ρ_s =2000 kg/m^3, water density ρ_w=998.2 kg/m^3, solid grain bulk modulus K_s= 6.78 GPa, water bulk modulus K_w= 0.20 GPa, permeability k= .25 × 10^{-3} m/s. The Angle of internal friction and dilatancy are exactly the same as in Ref [5]. Table 1 lists other parameters which are obtained by calibration. The parameter γ is set to 1cm and m is set 1.5.

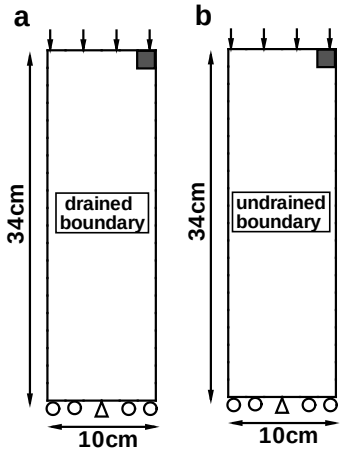

Figure 6: The biaxial specimen; geometry and boundary conditions (a) drained test, (b) undrained test

Table 1: Material parameters used in the computation

	σ_3'	Young modulus(E)	apparent cohesion (c_0)	softening modulus(H)
drained test on dense sand	100 kPa	2000 MPa	1 MPa	-15 MPa
drained test on dense sand	200 kPa	2500 MPa	2.5 MPa	-15 MPa
drained test on dense sand	400 kPa	2750 MPa	5 MPa	-15 MPa
drained test on dense sand	800 kPa	4000 MPa	8.5 MPa	-15 MPa
drained test on loose sand	100 kPa	600 MPa	.5 MPa	-1 MPa
drained test on loose sand	200 kPa	1000 MPa	1 MPa	-1 MPa
drained test on loose sand	400 kPa	1800 MPa	2 MPa	-1 MPa
undrained test on dense sand	100 kPa	2000 MPa	1 MPa	-15 MPa
undrained test on loose sand	800 kPa	2200 MPa	2.8 MPa	-1 MPa

In order to study the influence of the confining pressure on the material behavior of Hostun RF sand Desrues and Viggiani [5] varied the confining pressure in biaxial tests. The calculated and experimentally obtained normalized stress-strain curves for the different confining pressures are presented in Figure 7.The investigated range of confining pressure stress was 100–800 kPa for dense RF Hostun sand and 100–400 kPa for loose RF Hostun sand. The normalized stresses are nearly the same for experiment and the integral type nonlocal model enhanced by XFEM. Only the nonlinearity of the initial stiffness is underestimated in the calculations. A noticeable retardation of the localization and a decrease in the peak value are observed as confining stress increases. The stress drop after reaching the peak can be seen in figure 7a for dense sand. Figures 7b shows the results obtained in loose sand. The curve of the effective stress ratio vs. axial strain does not exhibit any sharp peak. In drained tests on loose (contractive) specimens, the onset of localization is clearly noted by a sudden change in the derivative and loss of regularity of the force-displacement curve.

The use of the determinant of the symmetric part of the acoustic tensor allows for representing the evolution of localized deformation. In figure 8, the development of shear band is shown by the contours of symmetric part of the acoustic tensor. Determinant of tensor were obtained at different states on the stress-strain response (Figs 8). As in the laboratory tests, in the numerical simulation, the shear band starts from the top of the specimen. The pattern of the shear

band is similar to what was observed in the laboratory tests [5]. The contours of symmetric part of the acoustic tensor indicated that shear banding initiates at, or shortly before peak. The stress drop is associated with the complete development of a shear band. Therefore, the inception and the development of the localization were described both qualitatively and quantitatively by local bifurcation theory.

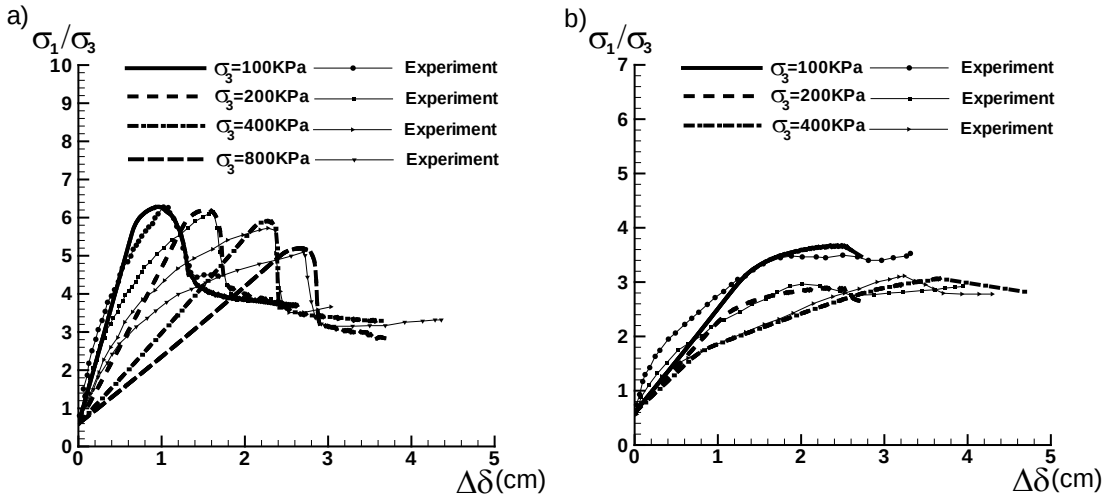

Figure 7: Experimental and numerical load-displacement curve for (a) dense sand and (b) loose sand under confining pressure 100-800kPa and drained condition

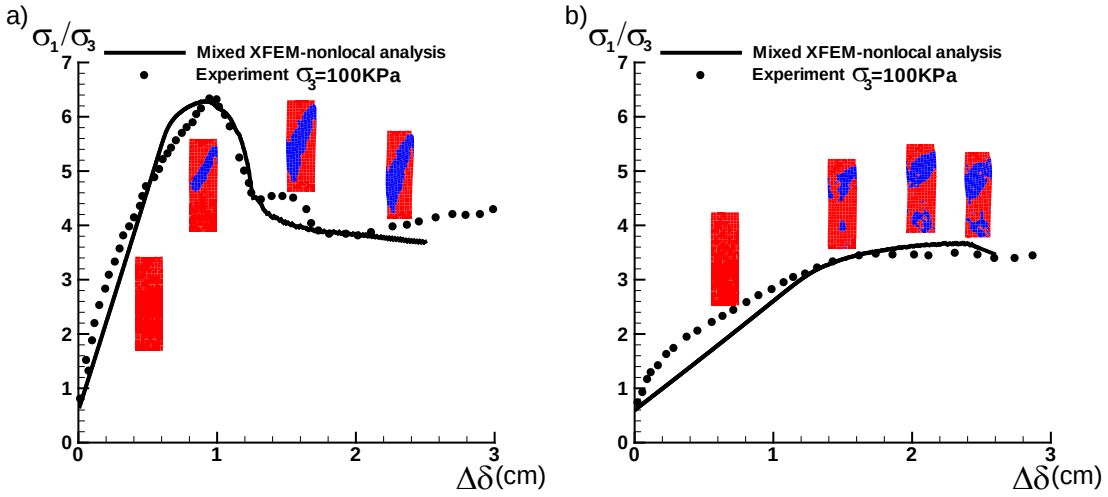

Figure 8: Experimental and numerical load-displacement curve for (a) dense sand (b) loose sand under confining pressure 100kPa and drained condition

Figure 9 and 10 present the effective plastic strain contours during a drained test on dense and loose Hostun RF sand under different confining pressure. The calculated shear band thickness and inclination are determined from the distribution of the effective plastic strain. In the calculations the shear band thickness does not change with increasing confining pressure. For both dense and loose sand, the numerically obtained inclination increases with increasing confining pressure. This is in accordance with the observations of Desrues and Viggiani [5] for biaxisal tests. For a given mean stress, shear bands are steeper in dense specimens than in loose specimens. In table 2,

the orientations are compared with the experimentally obtained shear band orientation. This is in good agreement with the observations made in drained biaxial tests on the dense sand by Desrues and Viggiani [4]. However, the calculated inclination of the shear band in loose sand is much lower than observed in the experiments. The underestimation of the shear band inclination is a well-known problem, which has been already observed for extended elastoplastic models [15]. For both dense and loose sand, Maximum effective plastic strain value decreased as confining pressure stress increased.

Figs. 11 and 13 present the nonlocal effective plastic strain and pressure contours for dense and loose sand under undrained condition. As shown in these figures, there is no significant difference between the drained and the undrained shear band orientations. The pore-water pressure distributions at different times are presented in Figs. 12 and 14. Water pressure concentration can be observed at the centre of the shear bands due to the plastic dilatant behavior of the dense sand and the plastic contractive behavior of the loose sand.

Several differences between the drained and undrained behavior of sand can be clearly seen. 1- In drained condition, strain localization occurs at axial strain levels lower than in the undrained case. 2- In both cases, the onset of localization and the development of localization were clearly revealed by the determinant of the symmetric part of the acoustic tensor. 3- In the drained tests, the maximum value of effective stress ratio is higher than in undrained conditions.

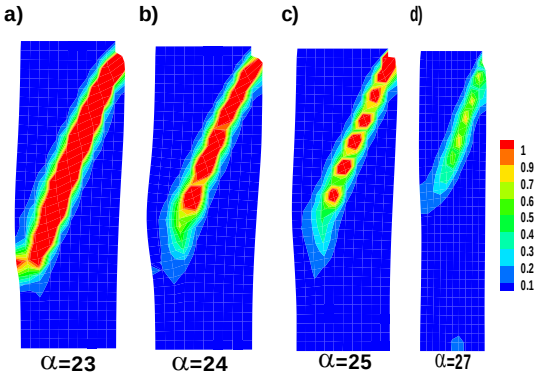

Figure 9: the effective plastic strain contour and orientation of the shear band for dense sand under (a) 100kPa (b) 200kPa (c) 400kPa (d) 800kPa confining pressure and drained condition

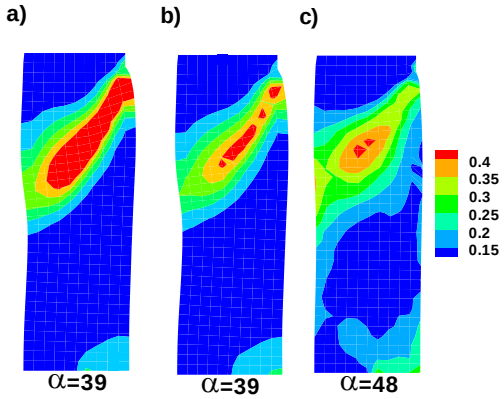

Figure 10: the effective plastic strain contour and orientation of the shear band for drained loose sand under (a) 100kPa (b) 200kPa (c) 400kPa confining pressure and drained condition

Table 2: Numerically and experimentally obtained shear band orientation

	σ_3'	numerically obtained orientation	experimentally obtained orientation [3]
drained test on dense sand	100 *kPa*	23	21
drained test on dense sand	200 *kPa*	24	24.5
drained test on dense sand	400 *kPa*	25	25.5
drained test on dense sand	800 *kPa*	30	30
drained test on loose sand	100 *kPa*	39	27.5
drained test on loose sand	200 *kPa*	39	28.5
drained test on loose sand	400 *kPa*	48	29
undrained test on dense sand	100 *kPa*	23	28.5
undrained test on loose sand	800 *kPa*	39	25.5

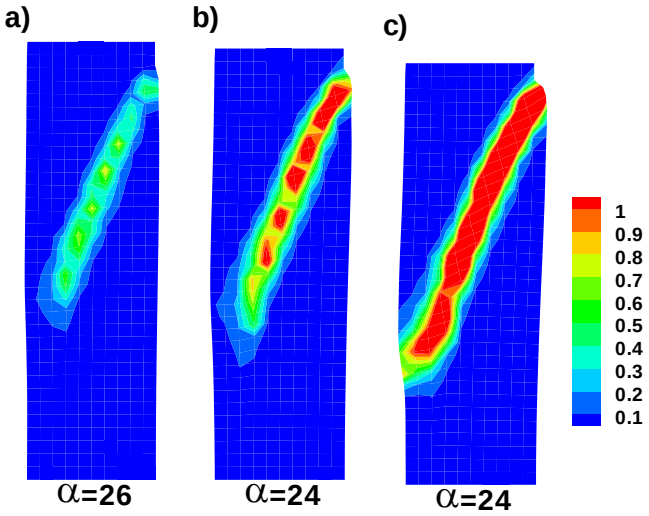

Figure 11: the effective plastic strain contour and orientation of the shear band for dense sand under 100kPa confining pressure and undrained condition; (a) Δδ=1cm (b) Δδ=1.5cm (c) Δδ=2cm

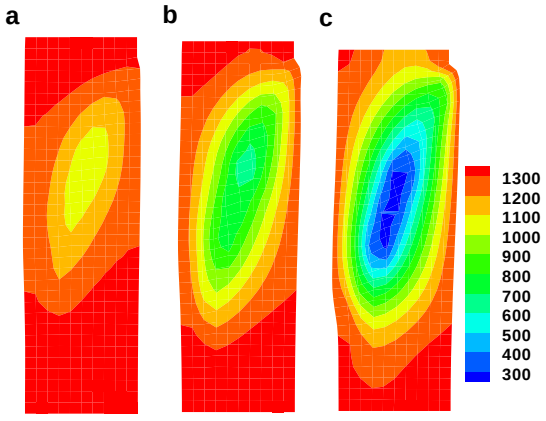

Figure 12: The distribution of pressure contour for dense sand under 100kPa confining pressure and undrained condition; (a) Δδ=1cm (b) Δδ=1.5cm (c) Δδ=2cm

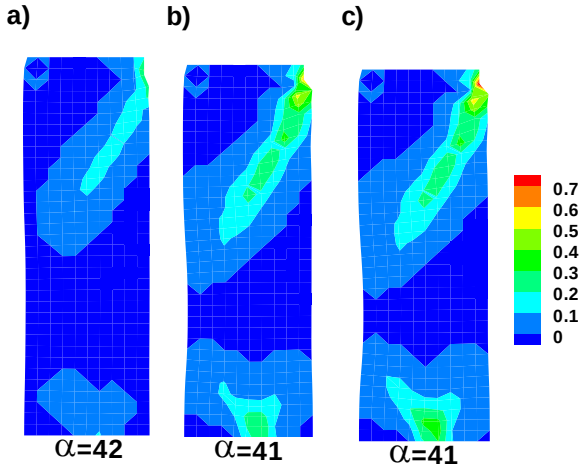

Figure 13: the effective plastic strain contour and orientation of the shear band for loose sand under 800kPa confining pressure and undrained condition; (a) Δδ=2.6cm (b) Δδ=3.2cm (c) Δδ=3.5cm

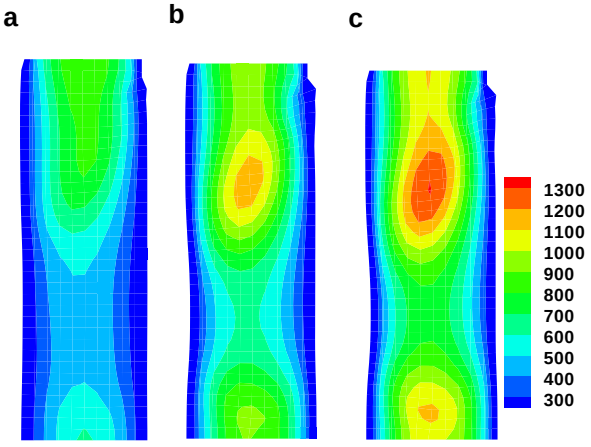

Figure 14: The distribution of pressure contour of the shear band for loose sand under 800kPa confining pressure and undrained condition; (a) Δδ=2.6cm (b) Δδ=3.2cm (c) Δδ=3.5cm

CONCLUSION

The integral type nonlocal model enhanced by XFEM method for granular materials like e.g. sands was presented by introducing a nonlocal plastic strain into the stress-strain relation. Governing equations were summarized in section 2. In section 3, XFEM was applied to the governing equations. Approximation of the displacement field in the localization band was improved by incorporating a set of special enrichments. The nonlocal model of Bazant and Lin [2] was extended in section 4. The tangent stiffness matrix was derived for the mixed integral type nonlocal-XFEM formulation. In section 5 a new method based on the local bifurcation theory was proposed for the initiation and growth criterion of the strain localization interface. In section 6, it was shown that the nonlocal model preserved the well-posedness of the governing equations in the post-localization regime and prevented pathological mesh sensitivity of the numerical results if the size of the element was smaller than γ. The mixed XFEM-nonlocal model

guaranteed mesh independence even if the size of the elements was larger than γ. In the other words, coarser mesh can be used for XFEM combined with a nonlocal model than when using only a nonlocal model. The computational effort required for the mixed XFEM-nonlocal model was less than for the nonlocal formulation because coarser mesh can be used in simulation. For the mixed XFEM-nonlocal model, the width and inclination of the shear band was obtained independently of element size. Finally, a dense and loose sand sample similar to a laboratory test was studied in detail to demonstrate the capability of the numerical model presented here to handle such situations. An agreement between the experimental observations and numerical results was obtained as far as the form of the shear band and the pore pressures are concerned. The influence of the mean stress level on the load–displacement curves can be represented qualitatively very well, but depends strongly on the exact calibration of the material parameters. Based on the results of the numerical simulation presented herein, the following conclusions can be drawn concerning drained and undrained compression of loose and dense Hostun RF sand. 1- The onset of the localization in form of shear bands is significantly affected by the confining pressure level. 2- The localization is retarded by increasing mean stress level.4- The orientation of shear zones increased with increasing pressure level. 3- Shear banding occurred in both loose and dense sand under undrained and drained condition. 4- The peak value of stress ratio in dense sand clearly depended on the confining stress. 5- The use of the determinant of the symmetric part of the acoustic tensor allowed for representing the evolution of localized deformation. 6- In the calculations the shear band thickness does not change with increasing confining pressure. 7- The numerical calculations shown that shear localization in granular bodies can be studied with the integral type nonlocal model enhanced by XFEM method.

REFERENCES

1. Bazant, Z., F. Lin and G. Pijaudier-Cabot (1987) “Yield limit degradation: non-local continuum model with local strain,” In the Proceedings of the computational plasticity, pp 1757–1780.

2. Bazant, Z.P. and F.B. Lin (1988) “Nonlocal yield-limit degradation,” International Journal for Numerical Methods in Engineering, Vol. 26, No. 8, pp 1805–1823.

3. Bazant, Z.P. and M. Jirasek (2002) “Nonlocal integral formulations of plasticity and damage survey of progress,” Journal of Engineering Mechanics, Vol. 128, No. 11, pp 1119-1149.

4. Belytschko, T. and T. Black (1999) “Elastic crack growth in finite elements with minimal remeshing,” International Journal for Numerical Methods in Engineering, Vol. 45, No. 5, pp 601-620.

5. Desrues J. and Viggiani G. (2004) “Strain localization in sand: an overview of the experimental results obtained in Grenoble using stereophotogrammetry,” International Journal for Numerical and Analytical Methods in Geomechanics, Vol. 28, No. pp 279–321.

6. Ehlers, W. , T. Graf and M. Ammann (2004) “Deformation and localization analysis of partially saturated soil,” Computer Methods in Applied Mechanics and Engineering, Vol. 193, No. 27-29, pp 2885–2910.

7. Eringen, A.C. (1981) “On nonlocal plasticity,” International Journal of Engineering Science, Vol. 19, No. 12, pp 1461–1474.

8. Eringen, A.C. (1983) “Theories of nonlocal plasticity,” International Journal of Engineering Science, Vol. 21, No. 7, pp 741–751.

9. Fries, T.P. and T. Belytschko (2010) “The extended/generalized finite element method: an overview of the method and its applications,” International Journal for Numerical Methods in Engineering, Vol. 84, No. 3, pp 253–304.

10. Jirasek, M. (1998) “Nonlocal models for damage and fracture comparison of approaches,” International Journal of Solids and Structures, Vol. 35, No. 31-32, pp 4133-4145.

11. Jirasek, M. and S. Rolshoven (2003) “Comparison of integral-type nonlocal plasticity models for strainsoftening materials,” International Journal of Engineering Science, Vol. 41, No. 13, pp 1553-1602.

12. Lewis, R.W. and B.A. Schrefler (1998) “The finite element method in the static and dynamic deformation and consolidation of porous media,” Wiley and Sons.

13. Liu, X., A. Scarpas and C. Kasbergen (2007) “A micropolar formulation of the Desai hierarchical model for elastoplastic porous media,” International Journal of Solids and Structures, Vol. 44, No. 9, pp 2695–2714.

14. Loret, B. and J.H. Prevost (1990) “Dynamic strain localisation in elasto(visco-)plastic solids. Part 1. General formulation and one-dimensional examples,” Computer Methods in Applied Mechanics and Engineering, Vol. 83, No. 3, pp 247–273.

15. Maier, T.h. (2003) “Nonlocal modeling of softening in hypoplasticity,” Computers and Geotechnics, Vol. 30, No. 7, pp 599-610.

16. Melenk, J.M. and I. Babuska (1996) “The Partition of Unity Finite Element Method: Basic Theory and Applications,” Computer Methods in Applied Mechanics and Engineering, Vol. 139, No. 1, pp 289-314.

17. Mokni M. and Desrues J. (1998) “Strain localization measurements in undrained plane-strain biaxial tests on Hostun RF sand. Mechanics of cohesive-frictional materials,” Mechanics of Cohesive-frictional Materials, Vol. 4, No. pp 419-441.

18. Pijaudier-Cabot, G. and Z.P. Bazant (1987) “Nonlocal damage theory,” Journal of Engineering Mechanics, Vol. 113, No. 10, pp 1512–1533.

19. Sluys, L.J. (1992) “Wave propagation, localisation and dispersion in softening solids,” Ph.D. thesis, Delft Univ.

20. Sulem, J. and I. Vardoulakis (1995) “Bifurcation Analysis in Geomechanics,” Blackie Academic and Professional.

21. Tejchman, J. (2002) “Patterns of shear zones in granular materials within a polar hypoplastic continuum,” Acta Mechanica, Vol. 155, No. 1–2, pp 71–95.

22. Zarinfar, M. and F. Kalantary (2013) “Numerical simulation of strain localization using mixed XFEM-integral type nonlocal model,” middle-east journal of scientific research, Vol. 16, No. 1, pp 73-87.

23. Zhang, H.W. and B.A. Schrefler (2000) “Gradient-dependent plasticity model and dynamic strain localization analysis of saturated and partially saturated porous media: one dimensional model,” European Journal of Mechanics - A/Solids, Vol. 19, No. 3, pp 503–524.

24. Zienkiewicz, O.C., A. Chan, M. Pastor, B.A. Schrefler and T. Shiomi (1999) "Computational Soil Dynamics with Special Reference to Earthquake Engineering," Wiley and Sons.

© 2013 ejge